RSC Advances

PAPER

View Article Online
View Journal | View Issue

Cite this: *RSC Adv.*, 2026, **16**, 7271

Acid-responsive metal organic frameworks with photothermal effects for osteoarthritis multiple therapy

Xin Feng,†[a] Yiqing Zhang,[a] Song Chen[a] and Yanfeng Ding *[ab]

Received 6th July 2025
Accepted 22nd December 2025

DOI: 10.1039/d5ra04833h

rsc.li/rsc-advances

Early osteoarthritis (OA) with reversible ability appears to lack features other than intense acute inflammation. Herein, we developed a pH-responsive metal organic framework (MOF) system based on phenylboronic acid (PBA) and O-hydroxyl pH-dependent reversible switches. Click chemistry enables a simple and environmentally friendly synthesis process and sensitive drug release procedure. Nanoparticles possess excellent photothermal conversion capabilities that enable thermal interventions alongside sustained drug release, thereby treating early OA in multiple ways. The results indicate that nanoparticles have high drug-loading capacity and can respond to the weakly acidic conditions in the OA microenvironment to release ellagic acid (EA) gradually. It can also significantly reduce inflammatory reactions induced by IL-1β. The high effectiveness of this compound therapy is comprehensively demonstrated by both *in vitro* and *vivo* evidence.

1. Introduction

Osteoarthritis (OA) is a chronic intraarticular inflammatory disease and is characterized by progressive loss of articular cartilage.[1,2] It is typically caused by the degeneration of articular cartilage[3,4] and progresses through three distinct stages before becoming severe. The initial phase of injury is characterized by acute inflammation,[5] significant cartilage edema, and a reduction in pH levels within the joint cavity. A minimal amount of glycosaminoglycan undergoes degradation,[6] while collagen remains intact.[7] This phenomenon can be attributed to the lack of enzyme-mediated cartilage degradation,[8,9] which underpins the potential for reversible treatment of early OA.[10–12] The middle stage of OA is marked by heightened activity of matrix metalloproteinases (MMPs) and type II collagenase,[13,14] resulting in significant enzymatic degradation of the cartilage matrix. This process is accompanied by degeneration and even apoptosis of chondrocytes, leading to an irreversible OA progression. In advanced stages, the joint function is completely compromised, with artificial joint replacement being the sole option for restoring mobility.[15,16]

Given the significant consequences of OA, a variety of treatment modalities have been proposed to alleviate pain and preserve joint function, including physical therapy, pharmacotherapy, and surgical interventions.[15,17] Recent guidelines have recommended thermal therapies as an effective form of physical therapy that markedly alleviates joint pain and protects joint functionality.[18,19] While oral nonsteroidal anti-inflammatory drugs (NSAIDs) represent a viable pharmacological option, their efficacy is limited by the sparse vascularization within the joints, necessitating higher dosages that may result in adverse gastrointestinal, cardiovascular, and renal effects. Intra-articular corticosteroid (CS) injections appear to be an effective therapeutic option. While corticosteroids can provide rapid pain relief, they may also induce chondrocyte apoptosis and contribute to the accelerated degradation of articular cartilage.[20] Hyaluronic acid (HA) injections are primarily indicated for patients with moderate arthritis who do not exhibit joint swelling; however, HA injections have limited efficacy in early osteoarthritis.[21]

A series of monostimulatory response particles for drug release have been studied; these nanoplatforms can release drugs for OA treatment under single-factor stimulation such as NO,[22] pH,[23,24] and reactive oxygen species (ROS).[24] Some natural molecules with anti-inflammatory properties, such as melanin,[25,26] *N*-acetyl-L-cysteine (NAC),[27,28] polyphenols,[29,30] and tempol,[31] have also been investigated for use in OA treatment. Recently, plant polyphenols have received great attention. Not only are their reserves second only to cellulose and lignin in nature,[32] but the rich active groups they contain demonstrate potential for chemical modification; however, they face the risk of rapid clearance by the joint synovium. Low drug load and single-drug delivery function make it difficult for these drug delivery systems to meet the needs of OA treatment. This could be due to the instability of synovial fluid in OA and drug release kinetics that are not modulated according to the severity of OA. Previous studies have shown that degenerative chondroinflammatory joints present

[a]*Department of Orthopedics, The Third People's Hospital Health Care Group of Cixi, Ningbo, 315300, China. E-mail: dingyanfeng1993@hotmail.com*
[b]*Guangxi Medical University, Nanning, 530000, China*
† Xin Feng contributed as first author.

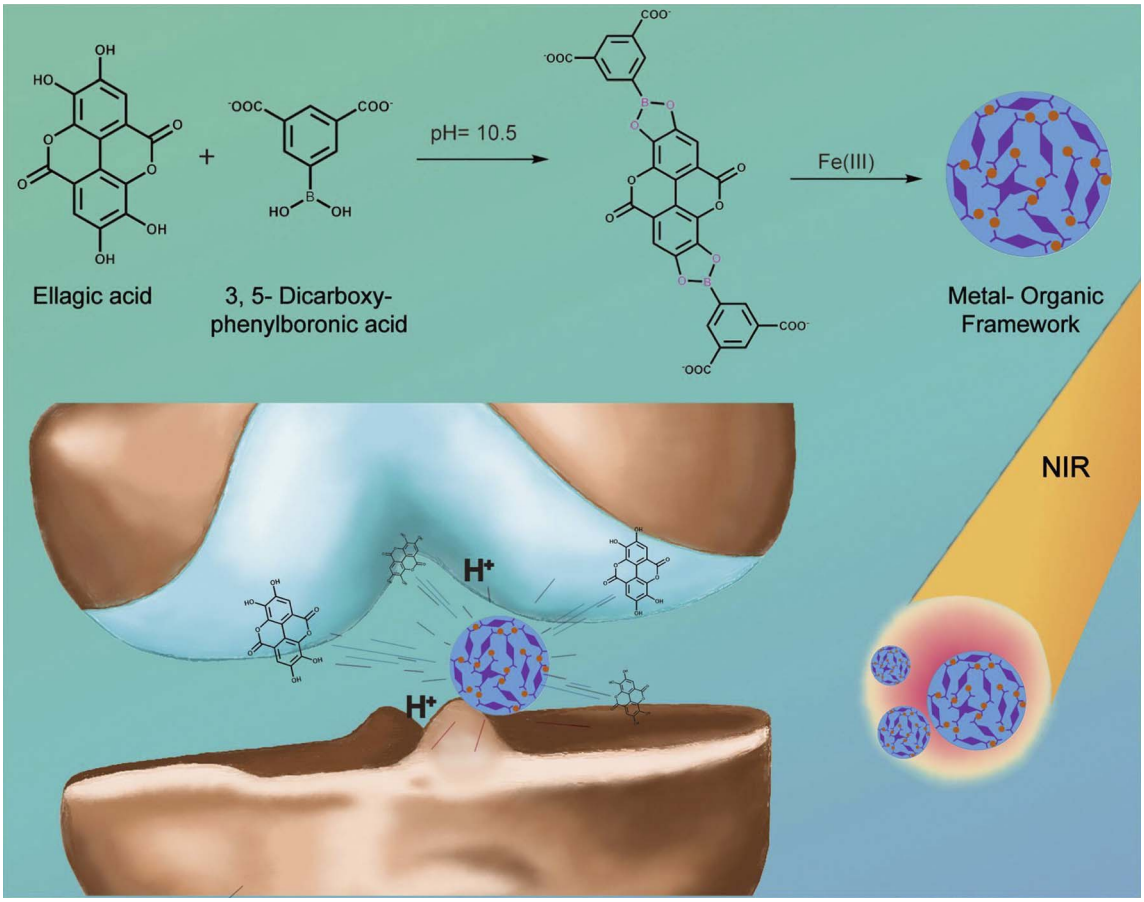

Fig. 1 Schematic of the fabrication of ellagic acid metal–organic frameworks (EA-MOFs) and the corresponding hypothesis on early OA treatment *via* MOF injection into the rat articular cavity.

a weakly acidic environment (as low as 6.0),[33–35] providing suitable triggering conditions for drug release. Therefore, in order to efficiently deliver the drug to the affected area of OA, avoid early leakage, and improve the therapeutic effect by controlling the release of the drug to inflammatory chondrocytes, it is necessary to develop a smart pH stimulus-responsive drug delivery system to achieve precise treatment of OA.

The pH-responsive drug release platform is again emphasized by researchers, because H^+ appears stably in early OA due to acute inflammatory response, while MMP-13 and type II collagenase do not. Acid-sensitive reaction groups, such as imine linkage (–C=N–),[36,37] hydrazone bond (–C=N–NH–),[38,39] amide bond (–CO–NH –),[40,41] and borolipid bond,[42,43] have received attention. The borolipid bond received more attention. The reaction of phenylboronic acid (PBA) and diol belongs to click chemistry. The B in the boric acid group has a 2p empty orbital (sp^2, triangle) and accepts hydroxyl groups to form borate ions (sp^3, tetrahedral) in alkaline environment. Furthermore, it is prone to nucleophilic reactions with nucleophilic groups, including hydroxyl and cyano groups. Under acidic conditions, the oxygen atom of borate esters protonates to form unstable oxonium. Oxonium has a strong ability to attract electrons, causing the B–O bond to break and generating hydroxyl and boric acid groups,[42] which means simpler reactions and greener synthetic systems. At the same time, the reactive pK_a is usually between pH 6.5 and 9.0,[44,45] ranked as PBA (7.8) > FPBA (7.2) > APBA (6.5–6.7),[46,47] which indicates that the drug release system is more sensitive to the environmental pH and can release large amounts of drug at pH 6.5, not 4.5.

In this study, we designed a metal organic framework (MOF) consisting of plant polyphenols rich in hydroxyl and PBA for the reversal treatment of early OA. As drug molecules constitute the MOF, it has a very high drug loading rate, which can reduce the number of injections in the articular cavity and the side effects caused by drug release residues. The higher pK_a of PBA and diol makes the particle extremely sensitive to H^+. In addition, the particles, which are black in color, provide excellent thermal interventions in near-infrared light and support OA interventions from multiple perspectives (Fig. 1, S1 and S2).

2. Materials and methods

2.1. Materials

Ellagic acid (EA, 98%), 3,5-dicarboxyphenylboronic acid (DBPB, 99%) and ferric chloride ($FeCl_3$, 99%) were purchased from Aladdin (China). Hydrochloric acid (HCl) and sodium hydroxide (NaOH) were supplied by Nanjing Reagent (China). Dimethyl

sulfoxide (DMSO) was purchased from Sigma-Aldrich (USA) and phosphate buffered saline (PBS) from SolarBio (China).

2.2. Synthesis of ellagic acid MOF

EA (0.3023 g, 1 mmol) was added with 20 mL of distilled water, with the pH adjusted to 10.5 using an NaOH solution (10 mM), and then centrifuged at 4000 rpm for 5 min to remove precipitated impurities. Similarly, DBPB (0.4199 g, 2 mmol) was added to 20 mL of distilled water, with the pH adjusted to 10.5 and using an NaOH solution (10 mM), and then centrifuged at 4000 rpm for 5 min to remove precipitated impurities. The above two solutions were mixed and placed in a shaking platform for 1 night, followed by the addition of 10 mL $FeCl_3$ aqueous solution (0.2 M) and continued shaking for another 1 hour. Subsequently, the mixture was heated in an oil bath at 60 °C for 4 hours, washed with distilled water (pH 8.0) and then centrifuged at 2000 rpm for 10 min for 3 times. Finally, the supernatant was discarded, and the precipitation was lyophilized (EA-MOF).

Fe–OH: added $FeCl_3$ solution (0.2 M) to NaOH solution (pH 10.5), a large amount of red sedimentation formed, these sedimentation treatments are the same as EA-MOF, take it as a potential product.

2.3. Characterization of EA-MOF

EA-MOF was characterized *via* infrared spectroscopy, and the crystal structure of the nanoparticles was characterized *via* powder XRD. The MOF nanoparticles was dispersed in water, 20 mg powder was added to 2 mL distilled water, and was ultrasonic for 10 min under water bath condition. Then, the nanoparticles were adsorbed with a copper mesh. The morphology of EA-MOF was observed *via* transmission electron microscopy (TEM, H-7650, Japan). Similarly, after the sample was added to the conductive glue, the surface morphology was observed *via* SEM (SM6700F, Japan). The particle-size distribution and zeta potential of micelles in suspension were measured using a particle-size instrument (Malvern Zetasizer Nano ZS90, UK). The specific surface area of nanoparticles was tested *via* Brunauer–Emmett–Teller (BET) N_2 adsorption (V-Sorb 2800 TP Pro).

2.4. Density of MOF in the water

Lyophilized EA-MOF powder (10 mg) was dissolved in 1 mL of distilled water (pH 8.0) for 10 min by ultrasonication and then centrifuged at 300 rpm for 30 min. Then, the centrifuge tube was placed in the centrifuge tube rack, and the density of the water was calculated using the formula $\rho = m/v$, after reading the volume of the underlying precipitation.

2.5. Photothermal reaction of EA-MOF

Lyophilized EA-MOF powder was prepared at turbidity levels of 50 μg mL^{-1}, 100 μg mL^{-1}, and 200 μg mL^{-1} and then cooled to room temperature after 10 min of ultrasonic treatment in the water bath. A near-infrared laser (Shconnet, China) with a wavelength of 808 nm and a power of 5 W was used to irradiate the suspension at a distance of 5 cm. The temperature was monitored using an infrared camera (Teledyne FLIR, USA) after a specific interval.

2.6. Drug-loading efficiency

EA-MOF (50 mg) was fully dissolved in 10 mL of HCl (pH 1.0), and the light absorption of the solution was measured at 336 nm using a microplate reader (Thermo Fisher Scientific, USA). At the same time, the optical absorbance of different concentrations was prepared using pure EA, and the standard curve of different concentrations–optical absorbance was established. The solution concentration was calculated according to the standard curve, and then the drug-loading efficiency of the particle was estimated.

2.7. Drug release studies

EA-MOF (50 mg) was added to 10 mL of different PBS solutions (pH 7.4, 7.0, 6.6, and 6.2) and placed in a shaker at 37 °C. The mixed liquid was centrifuged at 2000 rpm for 10 min every 12 hours, then 5 mL of supernatant was absorbed, and 5 mL of new PBS solution with the same pH was added.

The collected supernatant (0.5 mL) was taken and added with HCl (pH 1.0) to a constant volume of 8 mL. The absorbance of the supernatant was tested at 336 nm using a microplate reader, and the drug release was examined according to the standard curve.

Preparation of standard curve: 50 mg EA-MOF was added to 10 mL of HCl (pH 1.0) in the same manner. Under this condition, the EA-MOF immediately dissolved completely, and the solution exhibited a clear transparent yellow color. About 0.5 mL of the solution was taken and added with HCl (pH 1.0) to a final volume of 8 mL. The absorbance was measured at 550–250 nm using a microplate reader, with a maximum light absorption at 336 nm representing 100% drug release. The light absorption of the diluted solution of different multiples was measured, and the standard curve was drawn accordingly.

2.8. Degradation of EA-MOF

EA-MOF (50 mg) was added to 10 mL of different PBS solutions (pH 7.4, 6.4, and 5.4) and placed in a shaker at 37 °C. Then, the mixture was centrifuged for 10 min at 2000 rpm every 24 hours, and the supernatant was discarded, the sediment was lyophilized and the remaining powder mass was weighed. The lost mass was the amount of EA-MOF degradation, calculated as $D\% = (M_0 - M_n)/M_0$.

2.9. Chondrocyte isolation and culture

Chondrocytes were extracted from the knee joint of 5 days-old Sprague-Dawley (SD) rats. After dissecting the knee joints, the hyaline cartilage was cut and then digested at 37 °C with pancreatin-EDTA solution (SolarBio, China) for 1 hour and collagenase II (Sigma-Aldrich, China) for another 4 hours. Later, the liquid was centrifuged at a low speed of 500 rpm for 30 seconds, the supernatant containing chondrocytes was absorbed and added into the high glucose medium (DMEM, Gibco, USA), which contained 10% fetal bovine serum (FBS, Gibco, USA) and 1% Streptomycin- Penicillin (Solarbio, China). Ultimately, they

were cultured in an incubator at 37 °C, 5% CO_2 and 95% humidity.

2.10 Cytotoxicity *in vitro*

Chondrocytes (8×10^3 per well) were inoculated into 96-well plates. After 12 hours of adherent culture, the medium was replaced with medium containing different qualities of EA or EA-MOF. After 24 hours of continuous culture, the medium was aspirated and gently washed with PBS 3 times. Subsequently, 100 μL of the medium containing 0.5 mg mL^{-1} MTT was added to each well. After incubation for 4 hours, the supernatant was carefully removed and added with 100 μL DMSO. Finally, the light absorption of each well at 490 nm was measured using a microplate reader after 1 hour of shaking in the dark. The chondrocyte viability of EA and EA-MOF at different concentrations was calculated based on light absorption.

2.11. *In vitro* anti-inflammatory activity

Chondrocytes were cultured in 6-well plates. Each well was inoculated with 3×10^5 cells and added with 2 mL medium. After 12 hours of adherent culture, the medium with 5 ng mL^{-1} IL-1β was replaced. At the same time, 100 μg mL^{-1} of EA or EA-MOF was added. The chondrocytes with different treatment were divided into 4 groups: (1) W/O, only the medium was changed; (2) IL-1β, the medium was replaced with a medium containing 5 ng mL^{-1} IL-1β; (3) EA, the medium containing 5 ng mL^{-1} IL-1β + 80 μg mL^{-1} EA was replaced, but the medium containing only 5 ng mL^{-1} IL-1β was replaced again after 6 hours to simulate rapid drug clearance *in vivo*; and (4) EA-MOF, the medium was replaced with a medium containing 5 ng mL^{-1} IL-1β + 80 μg mL^{-1} EA-MOF. Each group was continuously cultured for 48 hours.

2.12. Live/dead assay

The 4 groups of chondrocytes cultured for 48 hours were prepared, and the live and dead cells were detected. After the culture medium of each group was removed, the cells were gently rinsed with PBS 3 times, and 2 mL of PBS containing 1 μM calcein-AM and 4 μM propidium iodide (PI) were added. The cells were incubated in the dark for 10 min, gently rinsed with PBS 3 times, and then observed and photographed using a fluorescence microscope (Olympus, Japan).

Flow cytometry assay using Alexa Fluor 488 Annexin V per PI Cell Apoptosis Kit (Invitrogen) was performed to detect and quantify apoptosis. The chondrocyte cells were digested using 0.25% Trypsin–EDTA after being incubated for 24 hours to obtain suspension cells. Then, 1×10^6 cells were taken and added with 400 μL buffer solution, 50 μL Annexin V and 50 μL PI. Afterwards, the cells were detected *via* flow cytometry after incubation for 10 min and washed with PBS. Annexin V-positive and PI-negative cells were scored as apoptotic. Double-stained cells were considered as necrotic/late apoptotic cells.

2.13. Quantitative real-time PCR (qRT-PCR)

Gene expression was examined *via* qRT-PCR. In detail, after treatment for 24 h, total RNA was isolated from chondrocytes using the HiPure Total RNA Mini Kit (Magen, China), in accordance with the manufacturer's instruction, and then the reverse transcription kit (Takara Bio, Japan) was used for reverse transcription. In the end, the qRT-PCR reactions were implemented using the LightCycler® 96 System (Roche, Swiss Confederation). The corresponding primers are presented in SI Table 1, and the expression levels of the gene were calculated using the $2^{-\Delta\Delta Ct}$ method and glyceraldehyde-3-phosphate dehydrogenase (GAPDH) serving as the internal reference.

2. 14. Immunofluorescence staining

The intracellular protein expression levels of MMP-3 and IL-1 were identified *via* immunofluorescent staining. Chondrocytes were fixed with 4% paraformaldehyde for 30 min after treatment for 48 hours and then gently rinsed with PBS 3 times for 2 minutes each time. After being soaked in 3% H_2O_2 for 15 min and gently rinsed with PBS 3 times, the goat serum was soaked for another 15 min to avoid non-specific binding. Subsequently, 200 μL of primary antibody MMP-3 (1 : 200 dilution, Boster, China) or IL-1 (1 : 200 dilution, Boster, China) was added to the cell slides and incubated at 4 °C overnight in the dark. Finally, after washing 3 times with PBS, FITC-Anti-Rabbit IgG (Boster, China) was added and incubated for 2 hours in the dark. The nuclei were stained with 4′,6-diamidino-2-phenylindole (DAPI) for 10 min. Images were captured using a fluorescence microscope (Olympus, Japan).

2.15. *In vivo* study

2.15.1. Induction of osteoarthritis in rats. Male SD rats were used as experimental animals to establish an arthritis model *via* anterior cruciate ligament transection (ACLT).[48] After the rats were anesthetized *via* intraperitoneal injection of pentobarbital sodium, the lateral skin of the patella was cut using a scalpel following disinfection with iodophor and separated layer by layer to access the joint cavity, after which the joint cavity was opened to remove the anterior cruciate ligament of the knee joint. Subsequently, the wound was sutured layer by layer, and then intramuscular injection of penicillin was administered to prevent infection.

After approval by the Ethics Committee, male rats weighing 200–250 g were randomly divided into 4 groups: (1) sham group, only the surface skin of the knee joint was incised; (2) OA + PBS group, one week after ACLT surgery, 100 μL PBS solution was injected into the joint cavity weekly; (3) OA + EA group, one week after ACLT surgery, 100−μL EA solution (100 μg mL^{-1}) was injected into the joint cavity weekly; (4) OA + EA-MOF group, one week after ACLT surgery, 100 μL EA-MOF solution (100 μg mL^{-1}) was injected into the joint cavity weekly. The joints were irradiated with an infrared laser (808 nm) at a distance of 5 cm for 10 minutes every day. The changes in knee joints were observed after 8 weeks of injection of drugs or PBS.

2.15.2. Collection of joint tissue and joint fluid. The rats were killed *via* intraperitoneal injection of excessive pentobarbital sodium after 8 weeks of treatment. After the rats were killed, their femur and tibiofibular were cut to completely remove the knee joint. Then, 150−μL PBS solution was injected

into the joint. After bending the knee joint repeatedly 10 times, about 100 μL of the joint fluid was extracted.

2.15.3. Macroscopic observation. The collected knee specimens were dissected, and the cartilage changes were assessed and scored in each group by three independent observers. As described by Pelletier *et al.*,[49] observers assessed the extent of articular cartilage lesion on a scale of 0 to 4. (0 = normal surface, 1 = slight tremor or yellow discoloration on the surface, 2 = erosion extending only to the superficial or intermediate layer, 3 = erosion extending deep, 4 = erosion extending to the subchondral bone).

2.15.4. Biochemical examination of joint fluid. The concentrations of MMP-3 and IL-1 in the joint fluid were determined using an ELISA kit (Meimian, China). The concentrations of MMP-3, IL-6 and carbonyl protein in each group were calculated by drawing the corresponding standard curve according to the reagent instructions.

2.15.5. HE and saffron-O/Fast Green staining. The knee specimens were fixed with 4% paraformaldehyde, embedded in paraffin and cut into 4 μm thick tissue slices, which were dyed according to the instructions for the HE staining kit. The simple description was as follows: after dewaxing and hydration, the nucleus was stained with hematoxylin, then the cytoplasm was stained with eosin, and finally, the slices were gently rinsed with PBS. Saffron-O/Fast Green staining was also performed according to the instructions. The nucleus was stained with hematoxylin first, then the bone with Fast Green, and finally, the cartilage with Saffron-O, with the latter gently washed with PBS and then sealed. A light microscope was used for observation and to take pictures. The sections were evaluated by three independent assessors according to the scoring criteria established by the Osteoarthritis Research Society International (OARSI).[50]

2.15.6. Immunohistochemical chemistry. After dewaxing and hydration, the sections were immersed in 3% H_2O_2 for 15 min to block endogenous peroxidase, gently rinsed with PBS and then incubated with goat serum for another 30 min. After being added with primary antibody, the sections were incubated at 4 °C overnight and gently rinsed with PBS. Later, they were incubated at room temperature for 20 min after the addition of the secondary antibody and then rinsed with PBS. Finally, the sections were dyed with DAB for 5 min, and the nucleus was stained with hematoxylin. After the transparent resin was sealed, the optical microscope was used for observation and to take pictures.

2.16. Biocompatibility *in vivo*

The effects of EA-MOF on erythrocyte sedimentation rate (ESR), erythrocyte stability, entrails and skeleton development were tested. Normal blood was obtained from rats. The tails were immersed in warm water at 45 °C for 15 s to dilate the caudal vein. Venous blood was drawn (10 mL) using a needle, and a 0.25-fold volume of 4% sodium citrate solution was immediately added for anticoagulation.

Normal saline (NS, 0.2 mL) or NS (0.2 mL) containing 100 μg mL^{-1} EA-MOF was added to 1.4 mL of blood and incubated at 37 °C for 2 hours before being added to the sedimentation tube for rest. The erythrocyte sedimentation distance was observed 6 hours later (ESR).

Blood (5 mL) was diluted with 10 mL NS and then centrifuged at 800 rpm for 30 min. This step was repeat 3 times to obtain concentrated red blood cells (CRBC). CRBC (200 μL) was transferred into EP tubes and then mixed with 1.3 mL of NS containing either 100 μg mL^{-1} EA, 100 μg mL^{-1} EA-MOF or distilled water (DW). After incubation for 2 hours, the morphology of the red blood cells was observed under a microscope. Then, the mixture was centrifuged at 3000 rpm for 5 minutes, and the color as well as the light absorption at 415 nm of the supernatant were examined using an enzyme label.

Following OA treatment, the hearts, livers, spleens, lungs and kidneys of the rats were harvested and fixed in 4% paraformaldehyde. The tissues were then embedded in paraffin and sectioned into 4 mm slices. After dewaxing and hydration, the sections were stained with HE dye, sealed, observed under an optical microscope and then photographed.

After OA treatment, the lower limbs of the rats were dissected below the tibia. The skin and subcutaneous fat were excised and fixed in anhydrous ethanol for one week, with the ethanol replaced every two days. Following degreasing in ethyl acetate for three days, a gradient alcohol hydration was performed over one week. Subsequently, immersion in 2% KOH solution for four hours was followed by staining with alizarin red ethanol saturated solution (with nine-fold volume of 1% KOH) for 48 hours. Then use distilled water washed every day for 1 week, and then soak in 3% H_2O_2 solution for 24 hours and hyalinization with gradient glycerin finally.

2.17. Statistical analysis

All the quantitative data were obtained in triplicate, and representative results were displayed. The values were expressed as mean ± standard deviation. Statistical comparisons among different groups were made *via* one-way ANOVA, and Student's *t*-test was conducted between the groups with significant comparisons. A p-value < 0.05 was considered statistically significant. All statistical analyses were performed using the SPSS 23.0 software.

3. Results and discussion

3.1. Characterization of EA-MOF

No obvious changes were observed when the EA solution (yellow) was mixed with DPBP solution (colorless), but after the $FeCl_3$ solution was added to the mixture, black film solid precipitates immediately appeared (Fig. S3 and S4). FTIR spectroscopy was performed to study the chemical structure of the products (Fig. 2A). The peaks at 1055 cm^{-1} and 1113 cm^{-1} are attributed to ester bonds (C–O–C) in EA; these absorption peaks also appear in EA-MOF (1033 cm^{-1} and 1109 cm^{-1}). The absorption peaks at 1684 cm^{-1} (C=O) and 928 cm^{-1} (–OH) are contributed by carboxyl group in DBPB, in EA-MOF, the peak at of C=O at 1697 cm^{-1} (blue shift), but the peak of –OH is disappear. The XRD results are presented in the Fig. 2B and S5, indicating that the particles possess a lamellar microstructure.

TEM images reveal that the EA-MOF nanoparticles have a uniform lamellar structure and measure approximately 100–200 nm (Fig. 2C). The morphology of nanoparticles was further investigated *via* SEM and was found to have a lamellar structure, and the various elements, such as B, C and O, were evenly distributed (Fig. 2D(i–iv). The DLS size measurement in distilled water indicated that the MOF had an average size of 211 nm with a poly-dispersity index of 0.349, indicating uniform NP size distributions (Fig. 2E). The zeta-potential measurements indicated that EA-MOFs were negatively charged (−27.7 mV) (Fig. 2F). The boron content of EA-MOF was 3.1% (m m^{-1}) by theoretical calculation, 4.9% by SEM test, and 5.17% by elemental analysis (SI Table 2). These results collectively confirm the successful synthesis of EA-MOF. From the results of N_2 adsorption BET (SI Table 3), the specific surface area of EA was 0.750348 m^2 g^{-1}, that of Fe–OH was 18.912070 m^2 g^{-1}, and that of EA-MOF was 143.208671 m^2 g^{-1}. The area of EA-MOF was larger than those of FE-OH and EA but smaller than that of common MOF (MOF-5:1000–1500 m^2 g^{-1}, MOF-801 600–800 m^2 g^{-1}), which could be due to the sheet-like structure.

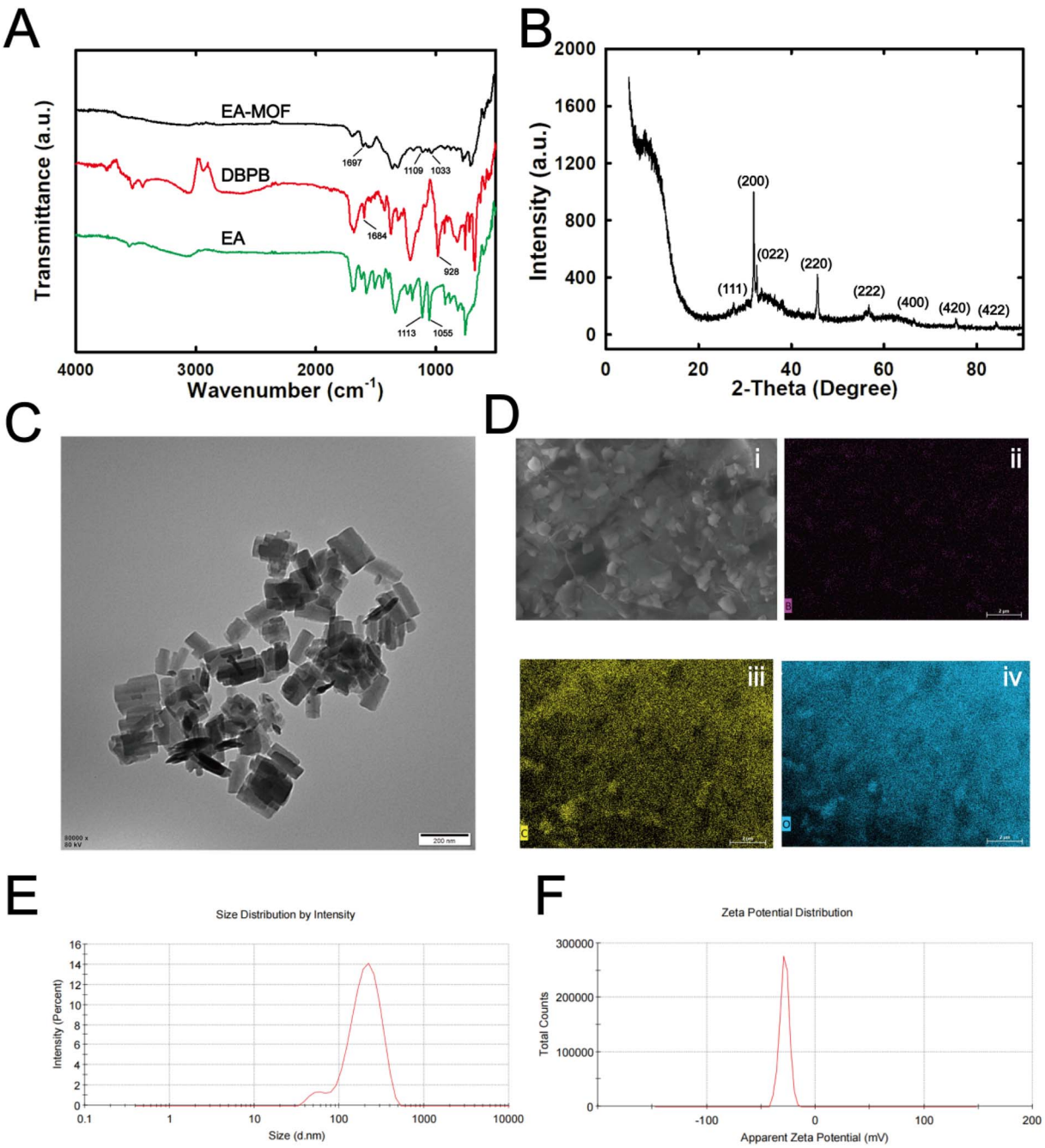

Fig. 2 Basic characterization of the EA-MOF. (A) FTIR results of EA, DBPB, and the EA-MOF. (B) XRD spectra of the EA-MOF. (C) TEM images of the EA-MOF. (D) SEM images of the EA-MOF. (E) Size of the EA-MOF. (F) Zeta potential of the EA-MOF.

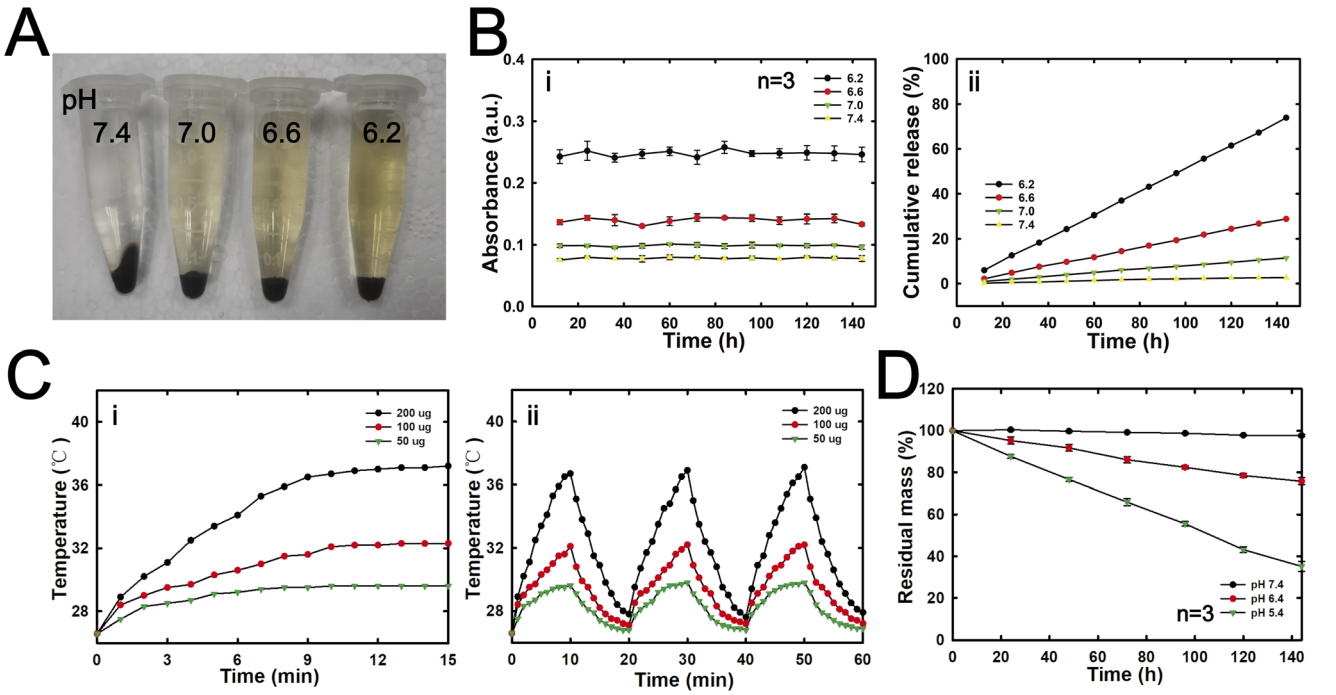

Fig. 3 Drug release properties and photothermal conversion of EA. (A) Image of the EA-MOF in different pH PBS buffer. (B) Drug release characteristics. (i). The amount of drug the particles release every 12 hours (100% is defined as the light absorption of the EA-MOF after the complete dissolution of excess HCl solution). (ii). Cumulative release. (C) Photothermal conversion of EA. (i). Temperature changes within 15 minutes in a solution with different EA concentrations. (ii). The temperature change of solution in infrared laser switching cycle. (D) *In vitro* degradation ratio of the EA-MOF in PBS buffers with different pH levels.

3.2. Density in water

MOF has a loose porous structure and a huge specific surface area. After dispersing it in water and subjecting it to centrifugation at a low speed, we measured its volume and calculated its water phase density as 10 mg mL^{-1} (Fig. S6). This result means that the nanoparticles are extremely loose and have a large surface area, with a physical basis that responds quickly to pH.

3.3. *In vitro* drug loading and release behavior

EA was directly involved in the form of the nanoparticles, so it has a vast drug loading. After the strong acid (HCl, pH 1.0) was completely dissolved, the light absorption characteristics of the solution were detected using an ultraviolet visible-light instrument. The results indicated that the solution had characteristic light absorption at 336 nm (Fig. S7A). Then, the light absorption of the solution was measured at 336 nm using a microplate reader, and the standard curve was drawn (Fig. S7B). The EA contained in the MOF was calculated as 41.7% (m m^{-1}) (SI Table. 2).

EA-MOF is very sensitive to pH, and its drug-release behaviour was detected under different conditions. The results are shown in Fig. 3A and B. Under physiological conditions (pH 7.4), the release amount of EA-MOF was extremely low, and nearly 0.5% of EA was released after 24 hours. Under sub-health conditions (pH 7.0), the drug release of nanoparticles significantly increased, with 1.3% accumulated after 24 hours. Under the condition of OA, when the pH dropped significantly, the release of nanoparticles increased rapidly; at pH 6.6 and 6.2, 4% and 6% were released, respectively. The cumulative release of EA over 144 hours was calculated, which was only 6.24% at pH 7.4, 86.82% at pH 6.2, and 13.02% and 40.42% at pH 7.0 and 6.6, respectively (Fig. 3B).

The results indicated that the EA-MOF we designed had a very high drug-loading rate and sensitive drug-release behaviors to pH changes.

3.4. Photothermal effect of EA-MOF

EA-MOF appears in black (Fig. S4) and has the ability to absorb light energy and convert it into heat energy. Herein, an infrared camera was used to observe the photothermal conversion of EA-MOF with different concentrations under near-infrared (NIR) conditions. As shown in Fig. 3C and S8, the liquid with different concentrations all underwent photothermal conversion under near-infrared light, and the temperature reached equilibrium about 10 minutes later (Fig. 3C(i)). The liquid with a low concentration of 50 μg mL^{-1} increased in temperature from 26.6 °C to 29.6 °C at the highest, the liquid with a high concentration of 200 μg mL^{-1} increased to 37.2 °C at the highest, and the liquid with a medium concentration increased to 32.3 °C (Fig. S8). This type of photothermal property is reversible. The liquid with different concentrations shows periodic temperature changes after three cycles of 10 minutes of illumination and 10 minutes of natural cooling. The liquid temperature reached its highest after 10 minutes of illumination and gradually cooled to room temperature after 10 minutes of cooling (Fig. 3C(ii)). The

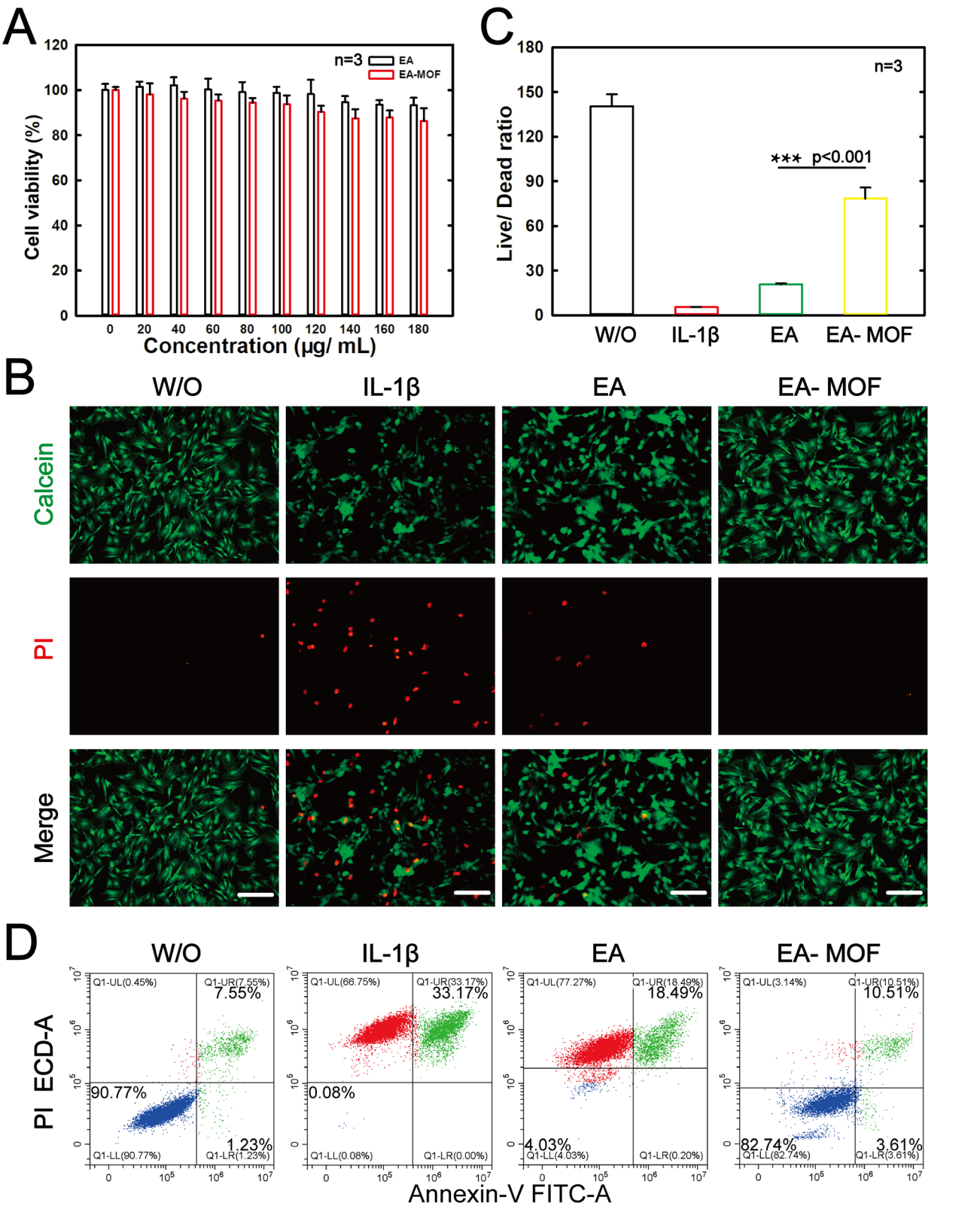

Fig. 4 Chondrocyte viability and protective effect of EA and the EA-MOF. (A) Chondrocyte cytotoxicity of microparticles examined *via* MTT assay. (B) Cell viability was determined *via* live/dead assay of the IL-1β- induced chondrocytes after treatment with EA or EA-MOF (100 μg mL^{-1}) for 24 h. The corresponding groups were W/O (normal chondrocytes), IL-1β (IL-1β-treated chondrocytes), EA (IL-1β-treated chondrocytes followed by EA incubation) and the EA-MOF (IL-1β-treated chondrocytes, followed by EA-MOF incubation) (scale bar: 200 μm). (C) Quantified results of chondrocyte live/dead staining (***$p < 0.001$). (D) Flow cytometry results.

results indicate that the nanoparticle has good photothermal properties and is useful in joint photothermal treatment.

3.5 MOF stability and degradation *in vitro*

EA-MOF is highly sensitive to pH, and it degrades and releases drugs in acidic environments. At pH 7.4, the mass of EA-MOF almost does not decrease, and the mass decrease is close to 2.4% after 144 hours. At pH 6.4, the mass decrease of nanoparticles increases significantly, and the mass decrease is 24.2% after 144 hours. At pH 5.4, the mass decrease is 64.9% (Fig. 3D). Compared with the loss of mass at pH 7.4, the mass of EA-MOF was reduced significantly at pH 6.4 and 5.4, respectively, indicating that the stability of particles was significantly reduced under acidic conditions, which was conducive to timely removal of particles in the joint.

3.6. Chondrocyte viability test

The cytotoxic effects of EA and EA-MOF on chondrocytes were analyzed *via* MTT. As shown in Fig. 4A, both EA and EA-MOF showed little cytotoxicity, and chondrocyte viability was above 90% at concentrations ranging from 0.5 to 100 μg mL^{-1}. We chose EA and EA-MOF with 100 μg mL^{-1} concentration for subsequent biological experiments, because the cell vitality was above 90% at this concentration. According to the results of live and dead cell staining (Fig. 4B), 5 ng mL^{-1} IL-1β significantly reduced the number of live chondrocytes (green), and the live-

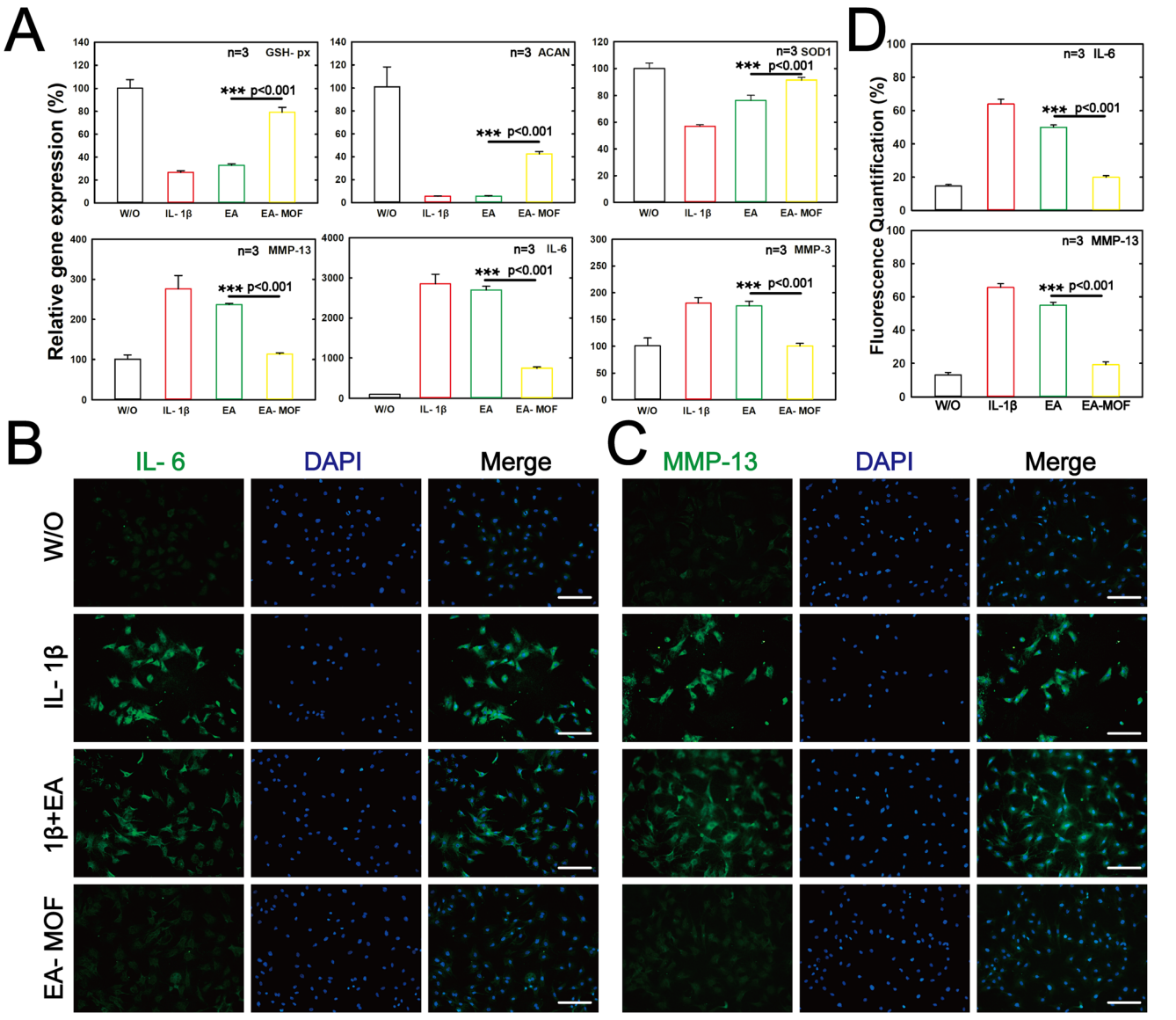

Fig. 5 Inhibition of the inflammatory factor expression of the IL-1β (10 ng mL^{-1})-treated chondrocytes by EA and the EA-MOF (100 mg mL^{-1}). (A) Relative mRNA levels of chondrogenic markers (ACAN), anti-inflammatory gene (GSH-px, SOD-1) and OA-relative genes (IL-6, MMP-13, and MMP-3). ($n = 3$, mean ± SD, ***$p < 0.001$). (B) The expression of IL-6 was detected *via* immunofluorescence staining. (C) The expression of MMP-13 was detected *via* immunofluorescence staining (scale bar: 100 μm). (D) Quantification of fluorescence after incubation with EA or EA-MOF for 24 h ($n = 3$, mean ± SD, and ***$p < 0.001$).

to-death ratio was 5.3. The number of living chondrocytes in the EA group was not significantly increased, and the survival per death ratio was 20.8. However, EA-MOF saved IL-1β-induced chondrocytes with a ratio of 78.3 (Fig. 4C). The results indicated that EA-MOF could effectively prevent the damage of chondrocytes caused by oxidative stress induced by IL-1β.

Cell flow cytometry also obtained similar results. As shown in Fig. 4D, in the EA group, the proportion of apoptotic cells (green) decreased from 33.17% to 18.49%, while in the EA-MOF group, the proportion of apoptotic cells dropped to 10.51%, and in the normal group, it was 7.55%. The results indicated that IL-1β induced a strong inflammatory response, and EA-MOF exerted a significant anti-inflammatory effect, effectively preventing damage to chondrocytes caused by IL-1β-induced oxidative stress. However, the EA group provided limited protection for chondrocytes.

3.7 Action of EA-MOF on IL-1β-induced chondrocytes

After 24 hours of co-culture with IL-1β, the effect of EA-MOF on IL-1β-induced chondrocyte inflammation was studied by detecting the expression levels of OA inflammatory genes MMP-13, IL-6, and MMP-3; anti-inflammatory genes SOD-1 and GSH-px; and cartilage matrix gene ACAN. The expression of the OA inflammatory gene in the IL-1β group was the highest in all groups, and those of IL-6, MMP-13 and MMP-3 significantly increased by a factor of 28.51-fold, 2.76-fold, and 1.80-fold, respectively, compared with those in the normal control group (Fig. 5A). After transient EA treatment, the expressions of inflammatory genes were slightly reduced, but those of IL-6, MMP-13 and MMP-3 still increased by 26.98-fold, 2.37-fold and 1.75-fold, respectively. However, after continuous treatment with EA-MOF, the expressions of inflammatory genes were significantly reduced; those of IL-6, MMP-13 and MMP-3 only increased by 7.50-fold, 1.14-fold and 1.01-fold, respectively.

Anti-inflammatory genes SOD-1 and GSH-px were significantly inhibited in the IL-1β group. Compared with normal control group, in the IL-1β group, SOD-1 expression was 0.57-fold of normal group, GSH-px expression was 0.27-fold, temporary treatment of EA group SOD-1 expression was 0.76-fold of normal group, GSH-px expression was 0.33-fold, on the contrary, after treatment with EA-MOF, related anti-inflammatory genes were significantly restored, the expressions of SOD-1 and GSH-px were 0.91-fold and 0.79-fold, respectively. The expression level of ACAN, a vital gene secreted by the cartilage matrix, was significantly inhibited under the action of IL-1β. The expression level of ACAN was 0.05-fold relative to the normal group, and that of ACAN was only 0.06-fold in the EA group, while the expression level of ACAN in the EA-MOF group recovered to 0.43-fold. These changes in gene expression levels suggested that EA-MOF inhibited the expression of IL-1β-upregulated inflammatory factors and improved the expression of anti-inflammatory factors in the presence of IL-1β while maintaining the chondrocyte phenotype and saving the loss of cartilage matrix induced by IL-1β.

MMP-13 and IL-6 play an essential role in cartilage degeneration induced by OA. The effect of EA-MOF on the protein expressions of MMP-13 and IL-6 in IL-1β-induced

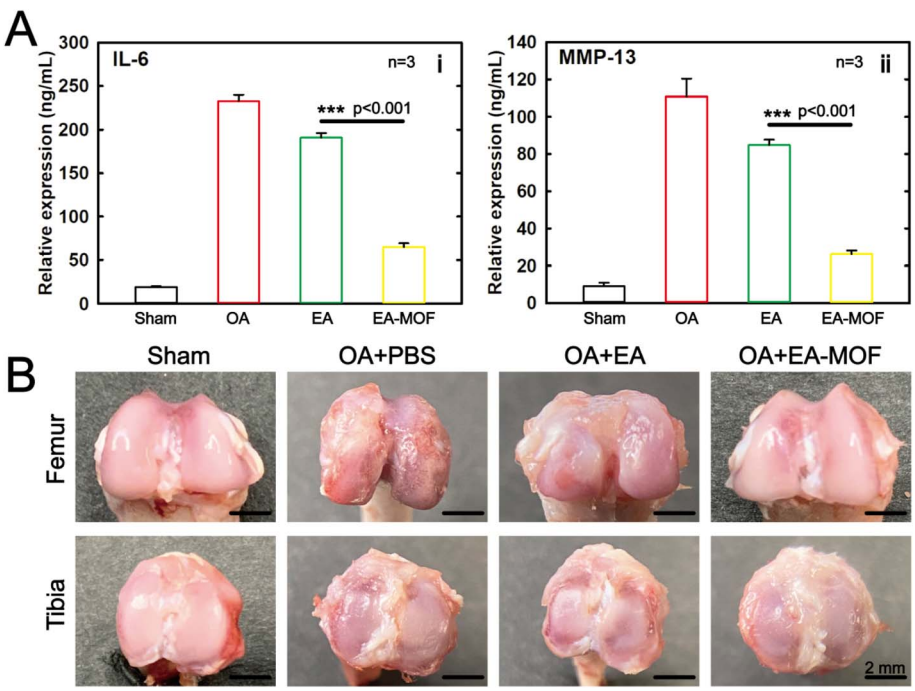

Fig. 6 OA therapeutic effects of EA and the EA-MOF. (A) Inflammatory factor (IL-6 and MMP-13) expression of the synovial fluid measured using the ELISA kit ($n = 3$, mean ± SD, and ***$p < 0.001$). (B) Macroscopic observation of the OA joint cartilage after EA or the EA-MOF treatment. The corresponding groups were sham (normal joint), OA + PBS (OA joint), OA + EA (OA joint treated with EA) and OA + EA -MOF (OA joint treated with the EA-MOF).

chondrocytes was studied *via* immunofluorescence staining. As shown in Fig. 5B and C, the control group all emitted weak fluorescence, indicating low-level secretion of MMP-13 and IL-6 in chondrocytes. Compared with the control group, both the IL-1β and EA groups showed strong green fluorescence, indicating that IL-1β strongly promoted the expressions of MMP-13 and IL-6, and transient EA treatment could not significantly inhibit the expressions of MMP-13 and IL-6. On the contrary, the fluorescence intensity in chondrocytes after treatment with EA-MOF was significantly decreased, and the fluorescence intensity decreased by 44.08% and 46.42%, respectively (Fig. 5D), compared with the IL-1β group. These findings suggest that EA-MOF maintains chondrocyte phenotype in the presence of IL-1β, inhibits the expression of IL-1β-upregulated inflammatory cytokines, and rescues IL-1β-induced cartilage matrix loss.

3.8. EA-MOF attenuate the progression of OA in rat

Knee fluid, femoral condyle and tibial plateau were collected after different treatments, and the mice were sacrificed at 6 weeks. The concentrations of MMP-13 and IL-6 in the synovial fluid were quantified using the ELISA kit (Fig. 6A and S9). The expressions of IL-6 and MMP-13 were significantly increased in the OA + PBS group compared with the sham group, whereas EA slightly reduced the expressions of IL-6 and MMP-13 by nearly 18.07% and 23.51% and EA-MOF significantly decreased these expressions by nearly 72.12% and 76.33%, respectively.

The articular cartilage was visually observed and compared with the smooth articular surface of the sham group; OA features represented by cartilage erosion, osteophyte formation and joint deformation were observed in the OA + PBS group. There was still extensive cartilage erosion after EA treatment. The cartilage lesions and erosion were significantly reduced after EA-MOF treatment

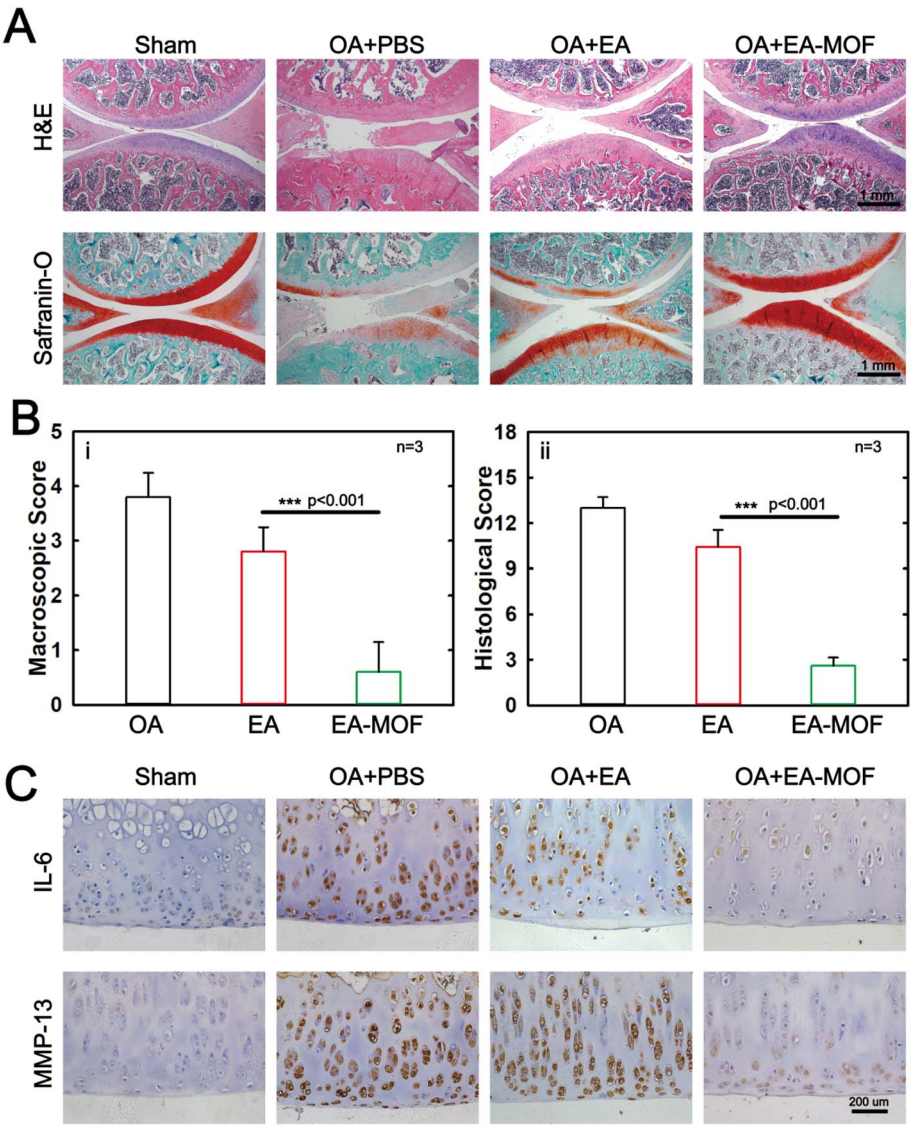

Fig. 7 Histological analysis of OA therapeutic effects by EA and the EA-MOF. (A) H&E staining (up) and Safranin-O/Fast Green staining (down). (B) The corresponding macroscopic scores (i) and histological scores (ii) ($n = 3$, mean ± SD, and ***$p < 0.001$). (C) Immunohistochemical staining of IL-6 and MMP-13 in the cartilage after treatment (scale bar: 100 μm).

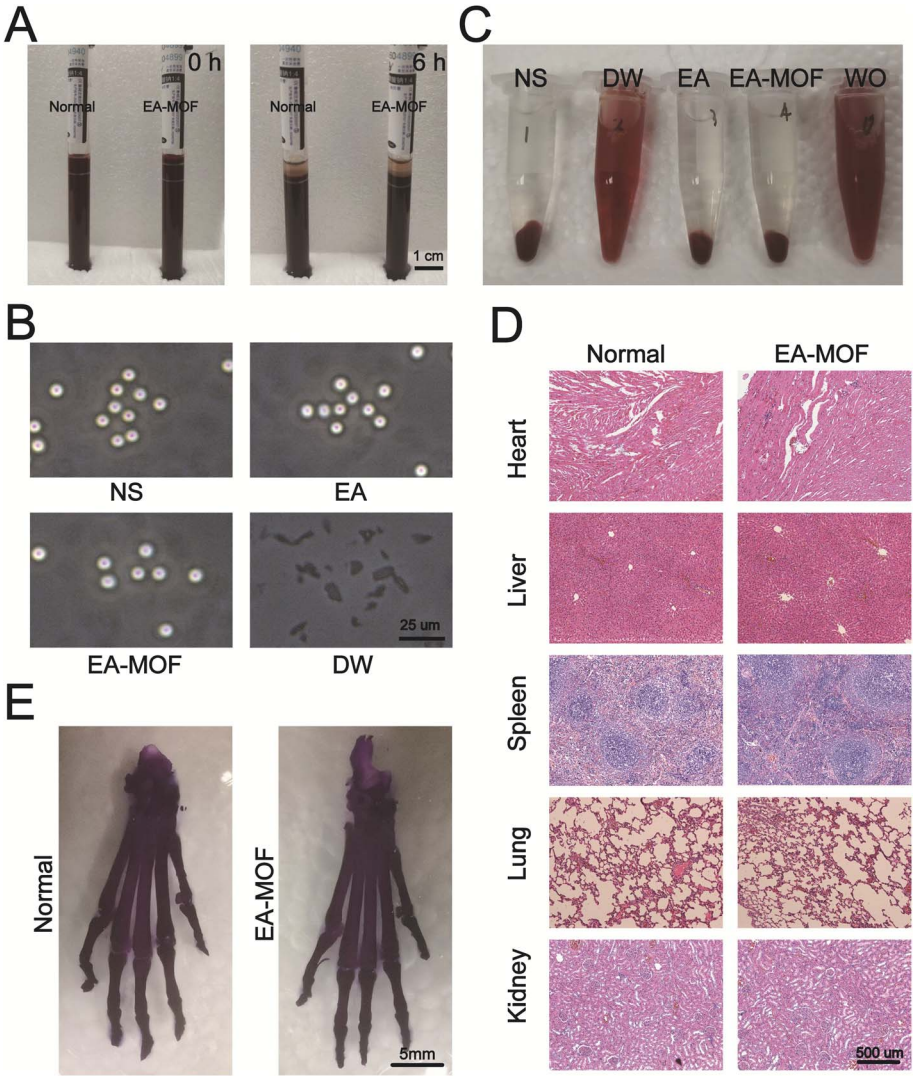

Fig. 8 . Biocompatibility *in vivo*. (A) The images of the sedimentation test. (B) The hemolysis test was conducted under a microscope. (C) The images of the hemolysis test. (D) The H&E staining of the laboratory animals' guts. (E) Alizarin red bone staining.

(Fig. 6B). Based on Pelletier's macro scoring, the cumulative scores of EA and EA-MOF were reduced by 16.32% and 84.21%, respectively, compared with the OA + PBS group (Fig. 7B i).

The cartilage tissue was evaluated *via* H&E and Saffron-O/Fast Green staining. As shown in Fig. 7A, the surface of the cartilage layer in the PBS group was rough, with vertical cracks, erosion, denudation, and deformation, consistent with the characteristics of OA. The surface of EA formation was rough, and there was still a large area of denudation. However, EA-MOF reversed the pathological changes, restoring the integrity of the tidal line, increasing the thickness of the cartilage layer, and enabling proteoglycan retention (Safranin-O staining-positive). Among all groups, the EA-MOF group achieved the greatest recovery of cartilage surface damage, complete cartilage structure, the strongest Saffron-O staining (red), and an 80% decrease in the cumulative score of OARSI, followed by the effect of EA, which decreased by 20% (Fig. 7B(ii)).

Immunohistochemical staining was used to evaluate inflammatory cytokines (MMP-13 and IL-6) in the cartilage. As shown in Fig. 7C, IL-6 and MMP-13 in the PBS and EA groups were strongly positive (dark brown). However, the EA-MOF group was negative, similar to the sham group. The results indicated that EA-MOF could effectively inhibit the progression of OA and exert a chondrocyte protective effect on OA joints.

3.9. Biocompatibility *in vivo*

The results of the sedimentation test are shown in Fig. 8A and S10(i). After 6 hours of natural sedimentation, the erythrocytes in the normal group sank about 5 mm, while those in the EA-MOF group sank about 5.5 mm. Similar results indicated that EA-MOF had a limited effect on erythrocyte sedimentation.

The results of the hemolysis experiment are shown in Fig. 8B and C, S10(ii), S11and S12. After 2 hours of incubation with NS, concentrated red blood cells still maintained a disc shape under microscope observation. After centrifugation, the supernatant was

colorless and transparent, and no hemoglobin overflow was detected in the supernatant. After 2 hours of incubation with distilled water (DW), the red blood cells were completely ruptured under the microscope. After centrifugation, a white cell membrane was seen at the bottom, and the supernatant was clear and exhibited a bright red color. The supernatant achieved strong light absorption at 386 nm. After the addition of NS containing EA and EA-MOF, the disk shape was maintained under the microscope (Fig. 8B and S11). After centrifugation, the supernatant could not be distinguished from the NS group by the naked eye (Fig. 8C). By measure the light absorption of the solution, 3.8% for EA and 6.8% for EA-MOF of red blood cells were ruptured, respectively (Fig. S12). The results indicated that EA and EA-MOF did not have the ability to induce rapid erythrocyte breakage.

The viscera of the EA-MOF group were collected and observed under the microscope to see whether the viscera were damaged. The results were as shown in the figure. Compared with the sham group (normal), no obvious damage was observed in the EA-MOF group, indicating that EA-MOF did not have the ability to affect the visceral function of rats (Fig. 8D).

Tissue-clearing staining enables visual observation of the skeletal system of the animal. The results are shown in the figure. The calcium-containing bone is stained red (alizarin red). As can be seen from the figure, there is no significant difference in the lower limb skeletal system of rats between the control group and the experimental group, indicating that EA-MOF had no effect on bone growth (Fig. 8E).

4. Conclusion

In summary, we successfully designed a novel MOF drug delivery platform to treat early OA. Due to its direct involvement in the composition of MOF, its drug loading capacity reaches 41.7% of the total weight, which reduces the toxicity caused by drug carrier residues, which decreases the number of articular cavity injections. Click chemistry enables simple and efficient synthesis steps and sensitive drug release procedures. Furthermore, it avoids cumbersome drug synthesis procedures and strict synthesis conditions. This nanoparticle has an extremely sensitive pH sensing ability and can adjust the drug release speed according to pH change in the joint cavity. It is conducive to the realization of personalized treatment. At the same time, the excellent photothermal conversion ability of nanoparticles can provide multiple treatments for arthritis.

The synthesized MOF particles have good biocompatibility, unlike hydrogels with low drug loading efficiency. These drug-assembled particles can offer a variety of therapeutic options and can intelligently regulate drug release. Compared with nanozyme, they avoid the risks of particle retention and heavy metal accumulation. This study provides hope for the clinical treatment of OA.

Ethical statement

All animal procedures were performed in accordance with the Guidelines for Care and Use of the Guiding Opinions on the Treatment of Laboratory Animals issued by the Ministry of Science and Technology of the People's Republic of China and the Laboratory animal-Guideline for ethical review of animal welfare issued by the National Standard GB/T 35892–2018 of the People's Republic of China and approved by the Animal Ethics Committee of the Animal Care & Welfare Committee of Guangxi Medical University.

Author contributions

Yanfeng Ding designed the study. Yanfeng Ding and Xin Feng substantially conducted the study and prepared the manuscript. Yanfeng Ding, Yiqing Zhang, Xin Feng and Song Chen contributed to the acquisition, analysis and interpretation of data. Yanfeng Ding drafted the article and revised it. All authors agreed to the final version to be published.

Conflicts of interest

The authors declare that no potential conflicts of interest.

Abbreviations

EA	Ellagic acid
DBPB	3,5-Dicarboxyphenylboronic acid
MOF	Metal–organic framework
OA	Osteoarthritis
NS	Normal saline
DW	Distilled water
MTT	3- (4, 5-dimethyl-2-thiazolyl)-2,5-diphenyl-2-H-tetrazolium bromide
ACLT	Anterior cruciate ligament transection
ESR	Erythrocyte sedimentation rate
CRBC	Concentrated red blood cells

Data availability

The datasets collected, obtained and analyzed during the current study are available from the corresponding authors upon request.

Supplementary information (SI) is available. See DOI: https://doi.org/10.1039/d5ra04833h.

Acknowledgements

This study funding come from individual, and has no specific name or number.

References

1 J. Martel-Pelletier, A. J. Barr, F. M. Cicuttini, P. G. Conaghan, C. Cooper, M. B. Goldring, S. R. Goldring, G. Jones, A. J. Teichtahl and J. P. Pelletier, Osteoarthritis, *Nat. Rev. Dis. Primers*, 2016, **2**, 16072, DOI: 10.1038/nrdp.2016.72.

2 L. A. Mandl, Osteoarthritis year in review 2018: clinical, *Osteoarthr. Cartil.*, 2019, **27**(3), 359–364, DOI: 10.1016/j.joca.2018.11.001.

3 I. Morales-Ivorra, M. Romera-Baures, B. Roman-Viñas and L. Serra-Majem, Osteoarthritis and the Mediterranean Diet: A Systematic Review, *Nutrients*, 2018, **10**(8), 1030–1040, DOI: 10.3390/nu10081030.

4 J. L. Whittaker, J. M. Losciale, C. B. Juhl, J. B. Thorlund, M. Lundberg, L. K. Truong, M. Miciak, B. L. van Meer, A. G. Culvenor, K. M. Crossley, E. M. Roos, S. Lohmander and M. van Middelkoop, Risk factors for knee osteoarthritis after traumatic knee injury: a systematic review and meta-analysis of randomised controlled trials and cohort studies for the OPTIKNEE Consensus, *Br. J. Sports Med.*, 2022, **56**(24), 1406–1421, DOI: 10.1136/bjsports-2022-105496.

5 J. Lieberthal, N. Sambamurthy and C. R. Scanzello, Inflammation in joint injury and post-traumatic osteoarthritis, *Osteoarthr. Cartil.*, 2015, **23**(11), 1825–1834, DOI: 10.1016/j.joca.2015.08.015.

6 S. Akizuki, V. C. Mow, F. Muller, J. C. Pita and D. S. Howell, Tensile properties of human knee joint cartilage. II. Correlations between weight bearing and tissue pathology and the kinetics of swelling, *J. Orthop. Res.*, 1987, **5**(2), 173–186, DOI: 10.1002/jor.1100050204.

7 A. Changoor, M. Nelea, S. Méthot, N. Tran-Khanh, A. Chevrier, A. Restrepo, M. S. Shive, C. D. Hoemann and M. D. Buschmann, Structural characteristics of the collagen network in human normal, degraded and repair articular cartilages observed in polarized light and scanning electron microscopies, *Osteoarthr. Cartil.*, 2011, **19**(12), 1458–1468, DOI: 10.1016/j.joca.2011.09.007.

8 M. A. Karsdal, K. Henriksen, M. G. Sørensen, J. Gram, S. Schaller, M. H. Dziegiel, A. M. Heegaard, P. Christophersen, T. J. Martin, C. Christiansen and J. Bollerslev, Acidification of the osteoclastic resorption compartment provides insight into the coupling of bone formation to bone resorption, *Am. J. Pathol.*, 2005, **166**(2), 467–476, DOI: 10.1016/s0002-9440(10)62269-9.

9 R. Stoop, P. M. van der Kraan, P. Buma, A. P. Hollander, A. R. Poole and W. B. van den Berg, Denaturation of type II collagen in articular cartilage in experimental murine arthritis. Evidence for collagen degradation in both reversible and irreversible cartilage damage, *J. Pathol.*, 1999, **188**(3), 329–337, DOI: 10.1002/(sici)1096-9896(199907)188:3<329::Aid-path371>3.0.Co;2-b.

10 E. M. Roos and N. K. Arden, Strategies for the prevention of knee osteoarthritis, *Nat. Rev. Rheumatol.*, 2016, **12**(2), 92–101, DOI: 10.1038/nrrheum.2015.135.

11 A. J. Palmer, C. P. Brown, E. G. McNally, A. J. Price, I. Tracey, P. Jezzard, A. J. Carr and S. Glyn-Jones, Non-invasive imaging of cartilage in early osteoarthritis, *Bone Joint J*, 2013, **95-b**(6), 738–746, DOI: 10.1302/0301-620x.95b6.31414.

12 H. Madry, E. Kon, V. Condello, G. M. Peretti, M. Steinwachs, R. Seil, M. Berruto, L. Engebretsen, G. Filardo and P. Angele, Early osteoarthritis of the knee, *Knee Surg. Sports Traumatol. Arthrosc.*, 2016, **24**(6), 1753–1762, DOI: 10.1007/s00167-016-4068-3.

13 M. A. Karsdal, S. H. Madsen, C. Christiansen, K. Henriksen, A. J. Fosang and B. C. Sondergaard, Cartilage degradation is fully reversible in the presence of aggrecanase but not matrix metalloproteinase activity, *Arthritis Res. Ther.*, 2008, **10**(3), R63, DOI: 10.1186/ar2434.

14 B. C. Sondergaard, K. Henriksen, H. Wulf, S. Oestergaard, U. Schurigt, R. Bräuer, I. Danielsen, C. Christiansen, P. Qvist and M. A. Karsdal, Relative contribution of matrix metalloprotease and cysteine protease activities to cytokine-stimulated articular cartilage degradation, *Osteoarthr. Cartil.*, 2006, **14**(8), 738–748, DOI: 10.1016/j.joca.2006.01.016.

15 J. N. Katz, K. R. Arant and R. F. Loeser, Diagnosis and Treatment of Hip and Knee Osteoarthritis: A Review, *Jama*, 2021, **325**(6), 568–578, DOI: 10.1001/jama.2020.22171.

16 J. T. Evans, J. P. Evans, R. W. Walker, A. W. Blom, M. R. Whitehouse and A. Sayers, How long does a hip replacement last? A systematic review and meta-analysis of case series and national registry reports with more than 15 years of follow-up, *Lancet*, 2019, **393**(10172), 647–654, DOI: 10.1016/s0140-6736(18)31665-9.

17 S. L. Kolasinski, T. Neogi, M. C. Hochberg, C. Oatis, G. Guyatt, J. Block, L. Callahan, C. Copenhaver, C. Dodge, D. Felson, K. Gellar, W. F. Harvey, G. Hawker, E. Herzig, C. K. Kwoh, A. E. Nelson, J. Samuels, C. Scanzello, D. White, B. Wise, R. D. Altman, D. DiRenzo, J. Fontanarosa, G. Giradi, M. Ishimori, D. Misra, A. A. Shah, A. K. Shmagel, L. M. Thoma, M. Turgunbaev, A. S. Turner and J. Reston, American College of Rheumatology/Arthritis Foundation Guideline for the Management of Osteoarthritis of the Hand, Hip, and Knee, *Arthritis Rheumatol.*, 2020, **72**(2), 220–233, DOI: 10.1002/art.41142.

18 L. Cantarini, G. Leo, C. Giannitti, G. Cevenini, P. Barberini and A. Fioravanti, Therapeutic effect of spa therapy and short wave therapy in knee osteoarthritis: a randomized, single blind, controlled trial, *Rheumatol. Int.*, 2007, **27**(6), 523–529, DOI: 10.1007/s00296-006-0266-5.

19 T. Ma, X. Song, Y. Ma, H. Hu, H. Bai, Y. Li and L. Gao, The effect of thermal mineral waters on pain relief, physical function and quality of life in patients with osteoarthritis: A systematic review and meta-analysis, *Medicine*, 2021, **100**(4), e24488, DOI: 10.1097/md.0000000000024488.

20 W. W. He, M. J. Kuang, J. Zhao, L. Sun, B. Lu, Y. Wang, J. X. Ma and X. L. Ma, Efficacy and safety of intraarticular hyaluronic acid and corticosteroid for knee osteoarthritis: A meta-analysis, *Int. J. Surg.*, 2017, **39**, 95–103, DOI: 10.1016/j.ijsu.2017.01.087.

21 V. Legré-Boyer, Viscosupplementation: techniques, indications, results, *Orthop. Traumatol. Surg. Res.*, 2015, **101**(1), S101–S108, DOI: 10.1016/j.otsr.2014.07.027.

22 P. Jin, C. Wiraja, J. Zhao, J. Zhang, L. Zheng and C. Xu, Nitric Oxide Nanosensors for Predicting the Development of Osteoarthritis in Rat Model, *ACS Appl. Mater. Interfaces*, 2017, **9**(30), 25128–25137, DOI: 10.1021/acsami.7b06404.

23 T. Jin, D. Wu, X. M. Liu, J. T. Xu, B. J. Ma, Y. Ji, Y. Y. Jin, S. Y. Wu, T. Wu and K. Ma, Intra-articular delivery of celastrol by hollow mesoporous silica nanoparticles for pH-sensitive anti-inflammatory therapy against knee osteoarthritis, *J. Nanobiotechnol.*, 2020, **18**(1), 94, DOI: 10.1186/s12951-020-00651-0.

24 Z. J. Zhang, Y. K. Hou, M. W. Chen, X. Z. Yu, S. Y. Chen, Y. R. Yue, X. T. Guo, J. X. Chen and Q. Zhou, A pH-responsive metal-organic framework for the co-delivery of HIF-2α siRNA and curcumin for enhanced therapy of osteoarthritis, *J. Nanobiotechnol.*, 2023, **21**(1), 18, DOI: 10.1186/s12951-022-01758-2.

25 J. Zhou, W. Liu, X. Zhao, Y. Xian, W. Wu, X. Zhang, N. Zhao, F. J. Xu and C. Wang, Natural Melanin/Alginate Hydrogels Achieve Cardiac Repair through ROS Scavenging and Macrophage Polarization, *Adv. Sci.*, 2021, **8**(20), e2100505–e2100518, DOI: 10.1002/advs.202100505.

26 C. Liu, Q. Zou, H. Tang, J. Liu, S. Zhang, C. Fan, J. Zhang, R. Liu, Y. Liu, R. Liu, Y. Zhao, Q. Wu, Z. Qi and Y. Shen, Melanin nanoparticles alleviate sepsis-induced myocardial injury by suppressing ferroptosis and inflammation, *Bioact. Mater.*, 2023, **24**, 313–321, DOI: 10.1016/j.bioactmat.2022.12.026.

27 Z. Meng, J. Liu, Z. Feng, S. Guo, M. Wang, Z. Wang, Z. Li, H. Li and L. Sui, N-acetylcysteine regulates dental follicle stem cell osteogenesis and alveolar bone repair via ROS scavenging, *Stem Cell Res. Ther.*, 2022, **13**(1), 466, DOI: 10.1186/s13287-022-03161-y.

28 B. Pedre, U. Barayeu, D. Ezeriņa and T. P. Dick, The mechanism of action of N-acetylcysteine (NAC): The emerging role of H(2)S and sulfane sulfur species, *Pharmacol. Ther.*, 2021, **228**, 107916–107937, DOI: 10.1016/j.pharmthera.2021.107916.

29 K. H. Myburgh, Polyphenol supplementation: benefits for exercise performance or oxidative stress?, *Sports Med.*, 2014, **44**(1), S57–S70, DOI: 10.1007/s40279-014-0151-4.

30 W. Jing, C. Xiaolan, C. Yu, Q. Feng and Y. Haifeng, Pharmacological effects and mechanisms of tannic acid, *Biomed. Pharmacother.*, 2022, **154**, 113561–113572, DOI: 10.1016/j.biopha.2022.113561.

31 R. Wang, J. Lu, J. Yin, H. Chen, H. Liu, F. Xu, T. Zang, R. Xu, C. Li, Y. Wu, Q. Wu, X. Fei, M. Zhu, L. Shen and J. Ge, A TEMPOL and rapamycin loaded nanofiber-covered stent favors endothelialization and mitigates neointimal hyperplasia and local inflammation, *Bioact. Mater.*, 2023, **19**, 666–677, DOI: 10.1016/j.bioactmat.2022.04.033.

32 S. Quideau, D. Deffieux, C. Douat-Casassus and L. Pouységu, Plant polyphenols: chemical properties, biological activities, and synthesis, *Angew Chem. Int. Ed. Engl.*, 2011, **50**(3), 586–621, DOI: 10.1002/anie.201000044.

33 M. Farr, K. Garvey, A. M. Bold, M. J. Kendall and P. A. Bacon, Signifcance of the hydrogen ion concentration in synovial fuid in rheumatoid arthritis, *Clin. Exp. Rheumatol.*, 1985, **3**(2), 99–104.

34 C. Li, H. Li, Q. Wang, M. Zhou, M. Li, T. Gong, Z. Zhang and X. Sun, pH-sensitive polymeric micelles for targeted delivery to infamed joints, *J. Contr. Release*, 2017, **246**, 133–141, DOI: 10.1016/j.jconrel.2016.12.027.

35 E. J. Goetzl, R. I. Rynes and J. S. Stillman, Abnormalities of respiratory gases in synovial fuid of patients with juvenile rheumatoid arthritis, *Arthritis Rheum.*, 1974, **17**(4), 450–454, DOI: 10.1002/art.1780170416.

36 T. Zhao, C. Liang, Y. Zhao, X. Xue, Z. Ma, J. Qi, H. Shen, S. Yang, J. Zhang, Q. Jia, Q. Du, D. Cao, B. Xiang, H. Zhang and X. Qi, Multistage pH-responsive codelivery liposomal platform for synergistic cancer therapy, *J. Nanobiotechnol.*, 2022, **20**(1), 177, DOI: 10.1186/s12951-022-01383-z.

37 L. Zhong, L. Xu, Y. Liu, Q. Li, D. Zhao, Z. Li, H. Zhang, H. Zhang, Q. Kan, Y. Wang, J. Sun and Z. He, Transformative hyaluronic acid-based active targeting supramolecular nanoplatform improves long circulation and enhances cellular uptake in cancer therapy, *Acta Pharm. Sin. B*, 2019, **9**(2), 397–409, DOI: 10.1016/j.apsb.2018.11.006.

38 X. Xu, B. Huang, Z. Zeng, J. Chen, Z. Huang, Z. Guan, M. Chen, Y. Huang and C. Zhao, Broaden sources and reduce expenditure: Tumor-specific transformable oxidative stress nanoamplifier enabling economized photodynamic therapy for reinforced oxidation therapy, *Theranostics*, 2020, **10**(23), 10513–10530, DOI: 10.7150/thno.49731.

39 E. Liu, M. Zhang, H. Cui, J. Gong, Y. Huang, J. Wang, Y. Cui, W. Dong, L. Sun, H. He and V. C. Yang, Tat-functionalized Ag-Fe(3)O(4) nano-composites as tissue-penetrating vehicles for tumor magnetic targeting and drug delivery, *Acta Pharm. Sin. B*, 2018, **8**(6), 956–968, DOI: 10.1016/j.apsb.2018.07.012.

40 S. Tang, A. T. Beattie, L. Kafkova, G. Petris, N. Huguenin-Dezot, M. Fiedler, M. Freeman and J. W. Chin, Mechanism-based traps enable protease and hydrolase substrate discovery, *Nature*, 2022, **602**(7898), 701–707, DOI: 10.1038/s41586-022-04414-9.

41 M. Qiu, Y. Tang, J. Chen, R. Muriph, Z. Ye, C. Huang, J. Evans, E. P. Henske and Q. Xu, Lung-selective mRNA delivery of synthetic lipid nanoparticles for the treatment of pulmonary lymphangioleiomyomatosis, *Proc. Natl. Acad. Sci. U. S. A.*, 2022, **119**(8), e2116271119–e2116271128, DOI: 10.1073/pnas.2116271119.

42 J. P. M. António, I. L. Roque, F. M. F. Santos and P. M. P. Gois, Designing Functional and Responsive Molecules with Boronic Acids, *Acc. Chem. Res.*, 2025, **58**(5), 673–687, DOI: 10.1021/acs.accounts.4c00691.

43 S. Kim, J. Lee, S. Im and W. J. Kim, Injectable immunogel based on polymerized phenylboronic acid and mannan for cancer immunotherapy, *J. Contr. Release*, 2022, **345**, 138–146, DOI: 10.1016/j.jconrel.2022.03.009.

44 V. Yesilyurt, M. J. Webber, E. A. Appel, C. Godwin, R. Langer and D. G. Anderson, Injectable Self-Healing Glucose-Responsive Hydrogels with pH-Regulated Mechanical Properties, *Adv. Mater.*, 2016, **28**(1), 86–91, DOI: 10.1002/adma.201502902.

45 J. Yan, G. Springsteen, S. Deeter and B. Wang, The relationship among pKa, pH, and binding constants in the interactions between boronic acids and diols—it is not as simple as it appears, *Tetrahedron*, 2004, **60**(49), 11205–11209, DOI: 10.1016/j.tet.2004.08.051.

46 V. Yesilyurt, M. J. Webber, E. A. Appel, C. Godwin, R. Langer and D. G. Anderson, Injectable Self-Healing Glucose-Responsive Hydrogels with pH-Regulated Mechanical

Properties, *Adv. Mater.*, 2016, **28**(1), 86–91, DOI: 10.1002/adma.201502902.

47 Y. Jun, S. Greg, D. Susan and W. Binghe, The relationship among pKa, pH, and binding constants in the interactions between boronic acids and diols—it is not as simple as it appears, *Tetrahedron*, 2004, **60**(49), 11205–11209, DOI: 10.1016/j.tet.2004.08.051.

48 T. Hayami, M. Pickarski, Y. Zhuo, G. A. Wesolowski, G. A. Rodan and L. T. Duong, Characterization of articular cartilage and subchondral bone changes in the rat anterior cruciate ligament transection and meniscectomized models of osteoarthritis, *Bone*, 2006, **38**(2), 234–243, DOI: 10.1016/j.bone.2005.08.007.

49 J. P. Pelletier, J. C. Fernandes, J. Brunet, F. Moldovan, D. Schrier, C. Flory and J. Martel-Pelletier, In vivo selective inhibition of mitogen-activated protein kinase kinase 1/2 in rabbit experimental osteoarthritis is associated with a reduction in the development of structural changes, *Arthritis Rheum.*, 2003, **48**(6), 1582–1593, DOI: 10.1002/art.11014.

50 R. W. Moskowitz, Osteoarthritis cartilage histopathology: grading and staging, *Osteoarthr. Cartil.*, 2006, **14**(1), 1–2, DOI: 10.1016/j.joca.2005.08.015.